sciendo

DOI 10.2478/ama-2022-0027

acta mechanica et automatica, vol.16 no.3 (2022)

EXPERIMENTAL AND NUMERICAL SMALL PUNCH TESTS OF THE 14Cr ODS FERRITIC STEEL

Krzysztof NOWIK*, Zbigniew OKSIUTA*

*Institute of Mechanical Engineering, Faculty of Mechanical Engineering, Białystok University of Technology, ul. Wiejska 45C, 15-351 Białystok, Poland

krzysztof.nowik@doktoranci.pb.edu.pl, z.oksiuta@pb.edu.pl

received 30 March 2022, revised 13 May 2022, accepted 16 May 2022

Abstract: Nowadays, various small specimen test techniques have gained wide popularity and appreciation among researchers as they offer undoubtful benefits in terms of structural material characterisation. This paper focuses on small punch tests (SPTs) performed on small-sized disc specimens to assess the mechanical properties of 14Cr oxide dispersion strengthened (ODS) steel. A numerical model was established to support experimental data and gain deeper insight into complex strain states developing in a deformed specimen. Modern evaluation procedures were discussed for obtaining mechanical properties from the small punch force-deflection response and were compared with the literature. Applicability and universality of those relations at different test conditions were also studied. It appeared that different ball diameters used had negligible influence on yield point but strongly affected ultimate strength estimation. It was found that friction belongs to decisive factors determining strain distribution in samples, as dry conditions increase the peak strain and move its location farther from the punch pole.

Key word: ODS ferritic steel, mechanical alloying, small punch testing, finite element method, yield stress, ultimate tensile strength

1. INTRODUCTION

Recently, various research methods using micro-samples have gained great importance and have become a new area of intensive research. Standard durability tests always involve large material losses, as they require relatively large samples. Therefore, in case of novel materials, it becomes very convenient to use micro-samples for testing, which are often obtained directly from the element during its working time [1,2,3,4].

One of the most remarkable techniques used to evaluate the mechanical properties of micro-sized specimens is the small punch test (SPT). Complex phenomena occurring during sample deformation along with severe plastic deformation spreading through the entire sample, often accompanied with necking and cracking, make the extraction of material parameters from the obtained force-displacement curve a difficult task, which is still an area of extensive research. SPT has gained wide attention in the field of nuclear materials, where the limitation to radiation exposure has a crucial priority [5,6,7].

Nowadays, we can observe a strong trend of gradual departure of fossil fuels in the energy sector. Researchers' efforts to develop future full-scale commercial fusion reactors are currently focused on the International Thermonuclear Experimental Reactor (ITER) megaproject, demonstrating the scientific and technological viability of fusion energy [8], advancing rapidly into the final construction stage [9]. The most critical obstacle is, however, selection of material, which would be able to withstand harsh working conditions.

Reduced activation ferritic (RAF) oxide dispersion strengthened (ODS) steels are primary candidates for the first wall of fusion reactors, due to their exceptional resistance to swelling and high thermal conductivity accompanied with low thermal expansion. Chemical composition of modern RAF ODS alloys is exclusively based on low activation elements, usually of type Fe-Cr-W-Ti-Y_2O_3, to ensure that radioactivity from the material decays to low levels in less than 100 years [10]. These alloys typically contain 12–16 wt.% Cr (usually 14% Cr) and are reinforced with ~0.3 wt.% of Y_2O_3, which ensures superior mechanical properties. Nowadays, ODS RAF steels are characterised by good tensile and creep strength, especially at elevated temperatures, and also with great oxidation and neutron irradiation resistance [11]. In the early stage of the ODS steel development, these materials contained simply pure Y_2O_3 oxide in the form of unfavourable, large-sized precipitates with a simple crystal structure [12]. To be an effective barrier to dislocation movement, the oxides should have a size of few nanometers and must be homogeneously distributed in the Fe matrix. Although the size of oxides can be optimised by adding Ti subsequently, the more recent studies have focused on modifying the chemical composition by adding different elements, such as Al, Hf, Zr and others [13]. Despite countless alternative fabrication routes towards ODS alloys being proposed, only powder metallurgy (PM) is currently established as the technique which allows the large-scale production of these materials.

This article reports experimental data and numerical simulations of SPTs performed on Fe-14Cr-2W-0.3Ti-0.3Y_2O_3 (wt.%) ferritic ODS alloys. ODS steels belongs to the group of structural nuclear materials with a great potential for use in future fusion reactors; so, their industrial importance is unquestionable. Experimental results have been supplemented by finite FEM analysis to gain deeper insight into the SP test and evaluate the impact of friction and test rig dimensions and material properties.

DOI 10.2478/ama-2022-0027

2. MATERIALS AND METHODS

Herein, an ODS steel powder with nominal composition of Fe-14Cr-2W-0.3Ti-0.3Y_2O_3 (wt. %) was mechanically alloyed (MA) for 42 h in a planetary ball mill Fritsch Pulverisette 6 under H_2 atmosphere, using the commercially available, high purity elemental powders. Mechanical grinding was conducted using 100 stainless steel balls, preserving the 10:1 ball-to-powder (BPR) weight ratio and constant rotation speed of 350 rpm. After MA, the powder was encapsulated in a soft steel can and then degassed and consolidated by hot isostatic pressing (HIP) at 1,150°C under the pressure of 200 MPa for 3 h. Afterwards, material was thermo-mechanically treated by hot pressing (HP) in a closed die at 850°C and finally annealed at 1,050°C for 1 h in Ar atmosphere. A transmission electron microscopy (TEM) image of HIP-HP-HT ODS steel consists of a fine (~400 nm) and relatively uniform distribution of equiaxed grains (Fig. 1), which indicates that the material can be regarded as isotropic. Details of the manufacturing process of studied herein and similar ODS alloys can be followed in the literature [14,15].

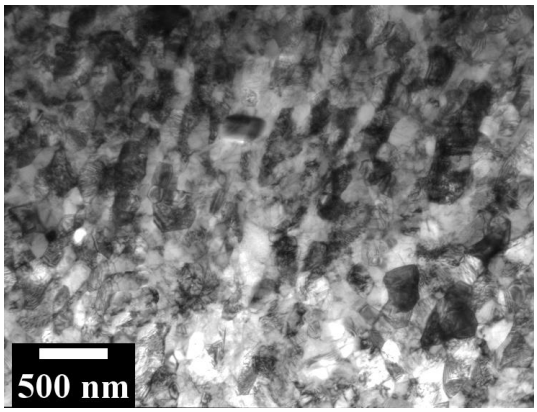

Fig. 1. TEM micrograph of 14Cr ODS steel used in this study. TEM, transmission electron microscope; ODS, oxide-dispersion strengthened

Basic elastic-plastic properties of the studied material were acquired from a uniaxial tensile test. Flat mini tensile specimens with dimensions of 2 × 5 × 27 mm with a gauge length of 6 mm were used at a strain rate of 1.0 × 10^{-4} s^{-1} using a MTS 858 testing machine, equipped with a 3542 Epsilon extensometer. Three samples were used to determine mean yield σ_0 and ultimate tensile strength, which were σ_{UTS} of 844 ± 27 and 953 ± 41 MPa, respectively, which proves the isotropy of HIP-consolidated material and, as a consequence, good reproducibility of tensile results (Tab. 1). Nominal stress σ_{nom} and strain ε_{nom} values obtained from uniaxial tensile test were converted to true stress-true strain using the following relations (Eqs. 1 and 2):

$$\sigma = \sigma_{nom}(1 + \varepsilon_{nom}) \quad (1)$$

$$\varepsilon = \ln(1 + \varepsilon_{nom}) \quad (2)$$

Tensile results are comparative with other ODS steels of similar chemical compositions reported by other authors [16,17]. According to De Sanctis et al. [18], shear modulus G of an ODS ferritic steel of similar chemical composition is 81 GPa. Therefore, we estimated Poisson's ratio value accordingly to $\nu = (E - 2G)/2G$, which equals to $\nu = 0.29 \approx 0.3$. Mean values of E and ν obtained from tensile tests were used in FEM simulation to specify elastic properties, whereas the classic metal plasticity model parameters were defined based on post-yield segment of the tensile curve (after subtracting the elastic strain). Fig. 2 shows the whole tensile curve, which is used to define plasticity, with insights focusing on the work hardening region.

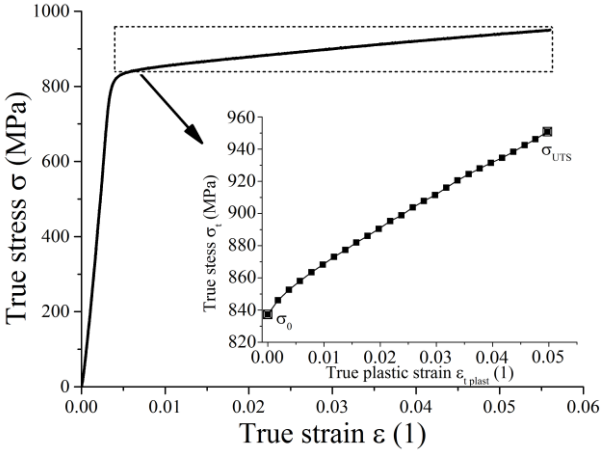

Fig. 2. True stress-strain tensile curve of studied ODS alloy used to define the plastic parameters. Insight shows the work hardening region, with squares representing data points tabularised in Abaqus. ODS, oxide-dispersion strengthened

Tab. 1. Basic elastic-plastic properties of the tested 14Cr ODS steel. These values were used in FEM simulations. ODS, oxide-dispersion strengthened; FEM, finite element method

Elastic-plastic properties	
***E* [GPa]**	208.5 ± 4.2
ν	0.3
σ_0 **[MPa]**	844 ± 27
σ_{UTS} **[MPa]**	953 ± 41
ε ***[%]***	5.48 ± 0.38

Developed in the 1980s, the SPT is one of the most commonly used methods for testing small volume samples [1,5]. Since SPT does not require large amounts of the material, it is especially useful when material availability is limited [19,20,21]. It is also practical to determine post-irradiation mechanical properties of nuclear materials since small volume samples limit radiation exposure [22,23]. Although this method has been exploited for almost 40 years, comprehensive standards for acquiring material data have only recently been established. Lack of universal methodology often makes obtained results incomparable. In Europe, the latest standardisation step for the SPT is the European standard EN 10371 "Metallic materials - Small punch test method" (2021). Also, the American National Institute of Standards and Technology (NIST) published a paper (internal report) [24] with guidelines of assessing the strength parameters using the SPT. The methodology of correlating the SPT and tensile results presented later in this work is in line with these documents and most scientific papers.

The essence of the SPT is based on pressing a spherical indenter at constant rate into a thin sample clamped between the dies [21]. The force F needed to push the ball into the material is

DOI 10.2478/ama-2022-0027

plotted as a function of the displacement u of the punch [5,25]. A number of specific values can be determined from the $F(u)$ curve, among which the most important are the following:

- F_{max}, the maximum force;
- u_m, the deflection at F_{max};
- F_e, the elastic-plastic transition force.

Due to easy accessibility, flat ⌀3 mm TEM specimens of 0.25 mm nominal thickness were chosen in this study. A constant load velocity of 0.5 mm/min was applied in Zwick Roell Z010 testing machine to press the ball into the specimen. An experimental setup exploited for the purpose of this research is shown in Fig. 3.

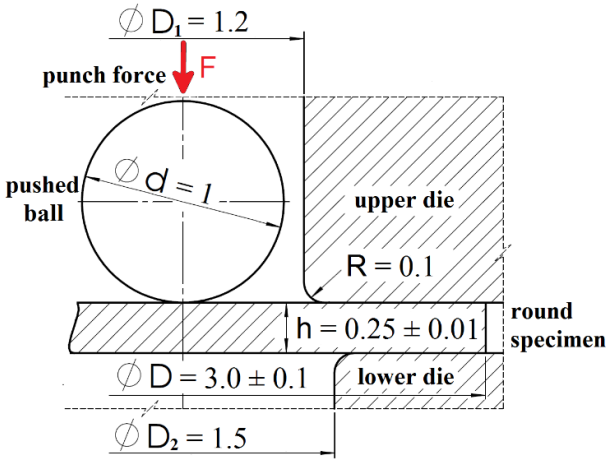

Fig. 3. Scheme of SPT setup used in the experiment. SPT, small punch test

There are mainly two different displacement measurement methods: top measurement and linear variable differential transducer (LVDT) measurement [26]. These non-identical setup combinations result in differences in the stiffness of each experimental SPT device and thus induce bias of the deflection. During SPT, when the displacement is measured as the displacement of the punch, the elastic displacement of the device and sample are added to the readings. Therefore, the elastic component of the total displacement in the raw load–displacement curves comprises both the material's and the machine's elastic response [27]. To take this error into account, the compliance correction of SPT system was performed, accordingly to procedures described in the literature [28], which is a common practice carried out for tensile and compression tests [29].

Thus, different empirical equations have been proposed to correlate SPT results with mechanical properties. Anyway, there is a complete agreement that the relationship between small punch "yield force" F_e and tensile yield strength σ_0 is linear, which can be expressed as Eq. 3 [5,30]:

$$\sigma_{0-SPT} = \alpha_1(F_e/h^2) + \alpha_2 \quad (3)$$

where the α parameters are the constants depending on test setup.

The small punch elastic-plastic transition point is not clearly defined since yielding in the specimen occurs heterogeneously [5]. As a consequence, the method of determining F_e is also a subject of debate, and different approaches have been suggested. The methodology of defining F_e in this paper is presented in Fig. 4. In this study, F_e was obtained according to a modified "two-secant" method proposed by Mao and Takahashi [31]. Normalising the equation with h^2 limits the thickness dependence of α parameters, as the force required for bending increases quadratically with its thickness [5].

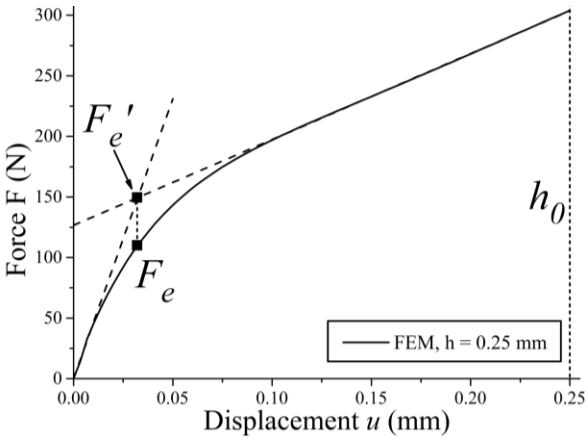

Fig. 4. Method of determining yield properties

Similar to yield strength estimation, various proposals have been evaluated to the correlate maximum SPT load (F_{max}) and the ultimate tensile strength σ_{UTS}. García et al. [30] found that Eq. 4 has low dependence on the thickness and gives the best estimate for a wide range of alloys:

$$\sigma_{UTS-SPT} = \beta_1(F_{max}/u_m h) + \beta_2 \quad (4)$$

Ultimate strength estimation is generally simple to utilize since both F_{max} and u_m are strictly defined and can be easily distinguished directly from $F(u)$ curve. β are the constant parameters, analogous to α in Eq. 3.

The FEM model, presented in Fig. 5, was developed in Abaqus. The model was designed as a two-dimensional axisymmetric assembly, which provided acceptable accuracy of calculations by rational computational time. An 8-node CAX8R elements were used to mesh the specimen part. As the indenter and both dies are multiple times stiffer than the specimen, they were modelled as infinitively stiff bodies.

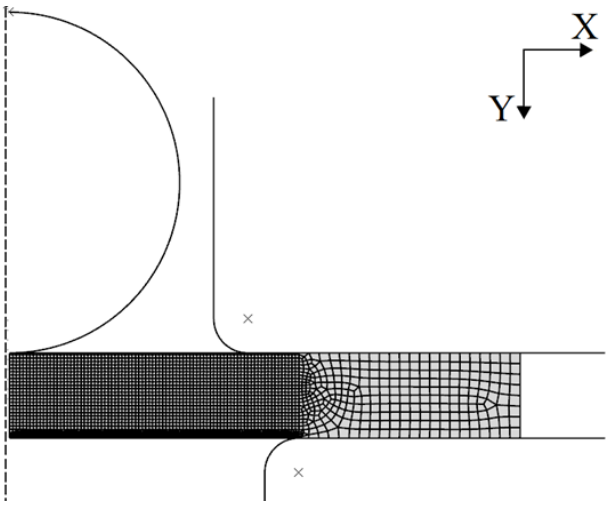

Fig. 5. FEM model of the SPT configuration in Abaqus. FEM, finite element method; SPT, small punch test.

DOI 10.2478/ama-2022-0027

3. RESULTS AND DISCUSSION

Numerical load-displacement curves are shown in Fig. 6. As depicted, friction coefficient has almost no effect on the initial force-displacement response until approximately up to the half of the curve. Fig. 7 shows the relationship between the μ and F_{max}. According to it, the increase in friction is accompanied by linear growth of the maximal force up to μ = 0.2. Beyond that, the increase in F_{max} becomes progressively smaller, and the relationship turns into nonlinear.

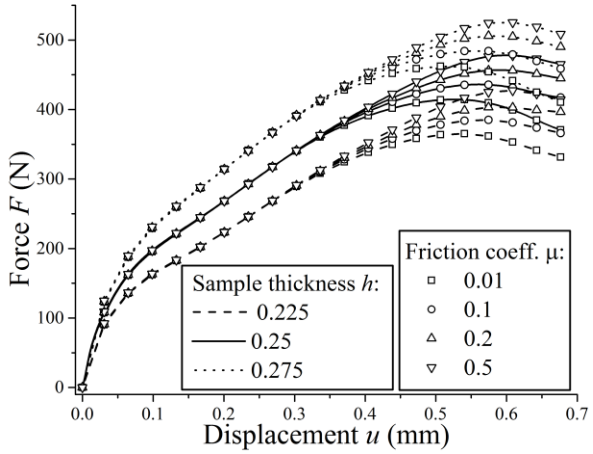

Fig. 6. Numerical force-deflection curves for various specimen thickness and friction coefficient

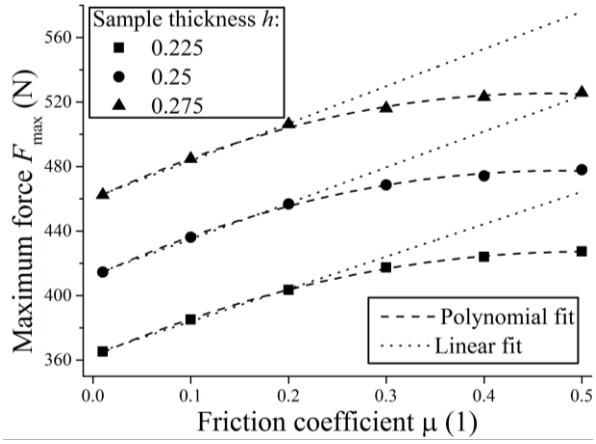

Fig. 7. The influence of friction coefficient value μ on obtained numerical maximal force F_{max}. Dotted line marks linear fit to the data

Along with specimen's deformation, biaxial stress and strain fields develop. Fig. 8 highlights the differences in plastic strain field evolution in samples deformed under contrasting friction conditions. Due to high stresses developed by pressing the ball against the elastic material, the specimen is exhibited to a serious level of deformation already at the onset of the test, as equivalent plastic strain ε^p reaches ~10 % with a punch displacement of just 0.01 mm (Fig. 8a). As the loading grows, plastic strain transfers to the bottom surface and localizes there (Fig. 8b). The effect of the friction on the strain field becomes visible only at the later stage of deformation. As compared in Fig. 8cd, high μ favours the accumulation of relatively large amounts of strain in a small region of the material, which is manifested macroscopically as a neck formed by prominent thinning at the strain localisation. Necking results in a smaller volume of high strain area and hence smaller growth of F_{max}, which explains the nonlinear trend of the $F_{max}(\mu)$ plot (Fig. 7).

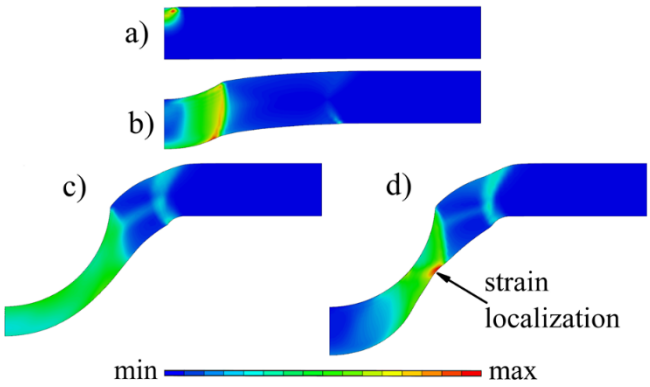

Fig. 8. Plastic strain equivalent plots at various deformation stages and friction conditions: (a) u = 0.068 mm, μ negligible, scale: [min 0; max 0.07]; (b) u = 0.136 mm, μ negligible, scale: [min 0; max 0.36]; (c): μ = 0.01 and (d): μ = 0.5: u = 0.68 mm, scale: [min 0; max 1.88]. See text for details

To gain deeper insight about plastic yielding of the material areas having direct contact with the indenter, ε^p curves at the specimen's reference node representing punch-specimen central point of contact were plotted in Fig. 9 as a function of punch displacement. According to it, strain immediately reaches ~0.02 at the moment of contact between the bodies and remains constant up to the displacement of ~0.2 mm, irrespectively of the assumed μ value, until the remaining surface of the specimen yet to come in contact with the punch, which deforms most easily due to absence of friction and wraps around the punch as it descends. As soon as the rest of the working surface of the punch comes with contact with the material, ε^p starts to rise again and the deformation at punch-specimen interface is the greater as the lower μ is. The reason for this is that the material in contact with the punch deforms easier under low friction conditions, as the resistance for the punch movement towards specimen is relatively low. In contrast, high frictional force favours sticking the punch to the material rather than deforming it, which postpones more deformation there and promotes more strain to occur at the non-contact areas.

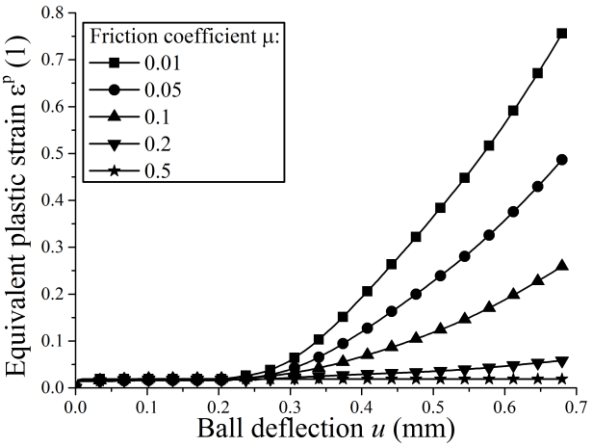

Fig. 9. Equivalent plastic strain at the punch-specimen pole

To elaborate the necking phenomenon in more detail, strain distribution along the bottom surface path (necking area) of the specimen at ultimate load was presented in Fig. 10. As the μ increases, not only the peak value of ε^p is found to be much higher but also its localisation in the material gradually moves away from the punch pole. A similar conclusion was made by other authors, who also observed that lubrication in experimental conditions reduces the ultimate load and moves the failure site closer to the pole of the punch [32].

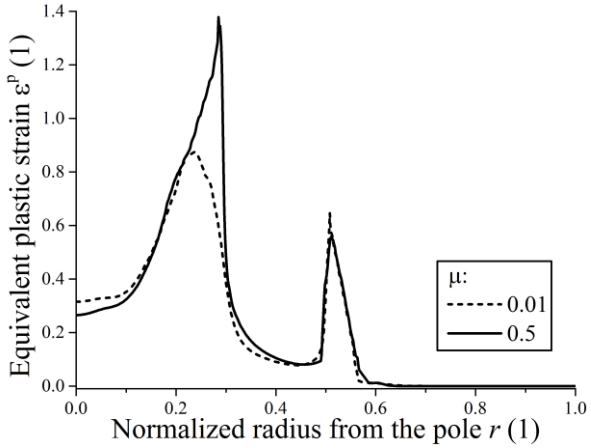

Fig. 10. Strain distribution along the bottom surface path of the specimen at ultimate load

In Fig. 11, numerical and experimental SPT curves are compared. Maximum force F_{max} and displacement at maximum force u_m values were extracted and listed in Tab. 2. Numerical curves with the friction coefficient of μ = 0.1 and μ = 0.2 were selected for comparison, as these values are within typical range for steel-steel friction pair and therefore should coincide well with experimental results.

Tab. 2. Maximum values of force Fmax along with their corresponding displacements um at Fmax for FEM and experimental curves (see Fig. 10). FEM, finite element method

Case	F_{max} [N]	u_m [mm]
FEM, μ = 0.1	433.7	0.561
FEM, μ = 0.2	452.8	0.592
Exp. 1	430.5	0.536
Exp. 2	443.7	0.538
Exp. 3	444.9	0.554
Mean experimental	439.7 ± 7.9	0.543 ± 0.010

Generally, the numerical and experimental results show good agreement. Experimental and FEM estimates of F_{max} are in very close agreement, both in case of μ = 0.1 and μ = 0.2. The scatter in the FEM and experimental F_{max} ranges from around 1% to 6%. In the case of the mean experimental F_{max} and u_m values (Tab. 2), μ = 0.1 is preferable (0.8% and 3.4% error for F_{max} and u_m estimation, respectively) and was used in further calculations.

Another interesting detail observed in Fig. 11 is that experimental and simulated force-displacement responses, although parallel, are not exactly overlapping, especially within the range of elastic region. As it is clear that the slope of the calculated curve is much steeper than its experimental counterparts, it can be stated that the stiffness of numerical data tend to be overestimated. The most probable explanation of this fact could be that the punch and dies were modelled as perfectly rigid, while in reality they are subjected to some deformations when transmitting the load and have defined compliance. The elastic region is also particularly influenced by various test inaccuracies, like sample thickness, settlement of experimental device parts, etc.

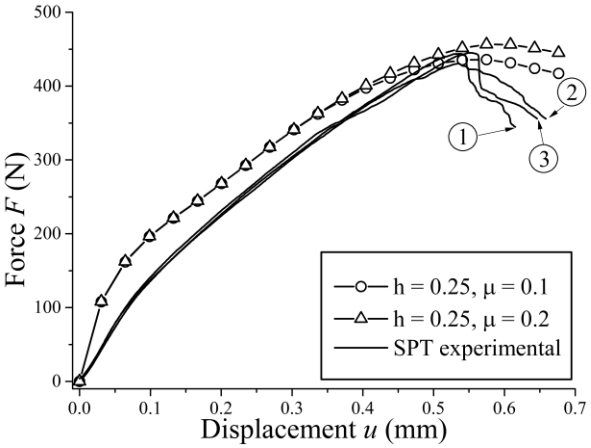

Fig. 11. Comparison of numerical and experimental small punch curves

The methods of assessing the characteristic material properties from the SPT data were also analysed. In line with [30,33], the intercept factors (α_2, β_2) of the linear equations Eqs. 3 and 4 were neglected, and they can be written in a simplified form:

$$\sigma_{0-SPT} = \alpha(F_e/h^2) \quad (5)$$

$$\sigma_{UTS-SPT} = \beta(F_{max}/u_m h) \quad (6)$$

Tab. 3. Values of the factors used in Eqs. 5 and 6 optimised for the current study. Literature values are also given

		F_e/h^2 [MPa]	α	$F_{max}/(u_m h)$ [MPa]	β
FEM, h = 0.225		1,631.8	0.513	3,019.2	0.315
FEM, h = 0.250		1,712.2	0.489	3,092.3	0.307
FEM, h = 0.275		1,797.9	0.466	3,123.3	0.302
Mean FEM		1,714.0 ± 83.1	0.488 ± 0.014	3,078.3 ± 53.5	0.309 ± 0.003
Exp. 1		1,957.1	0.428	3,212.7	0.296
Exp. 2		2,029.3	0.413	3,298.9	0.288
Exp. 3		2,171.6	0.386	3,212.3	0.296
Mean experimental (± SD)		2,052.7 ± 109.1	0.407 ± 0.012	3,241.3 ± 49.9	0.293 ± 0.005
Bruchhausen et al. [5]		-	α_1 = 0.382	-	β_1 = 0.326
			α_2 = 28.8		β_2 = -27.04
García et al. [30]		-	0.476	-	0.277
Campitelli et al. [28]	316L	970 ± 40	0.400 ± 0.012	-	-
	F82H	1,370 ± 80	0.388 ± 0.022	-	

DOI 10.2478/ama-2022-0027

Specific SPT parameters (α, β) derived from the experimental and FEM curves were collated in Tab. 3 and compared with the results obtained by other authors. Literature data included: an extensive study conducted on a broad range of metallic materials [30], other, covering austenitic and tempered martensitic steels [28] and finally, modified 9Cr-1Mo (Grade 91) ferritic-martensitic steel used in nuclear power plants [5]. The relationships attained between σ_0 and the F_e/h^2 were plotted in Fig. 12 along with results provided by other authors.

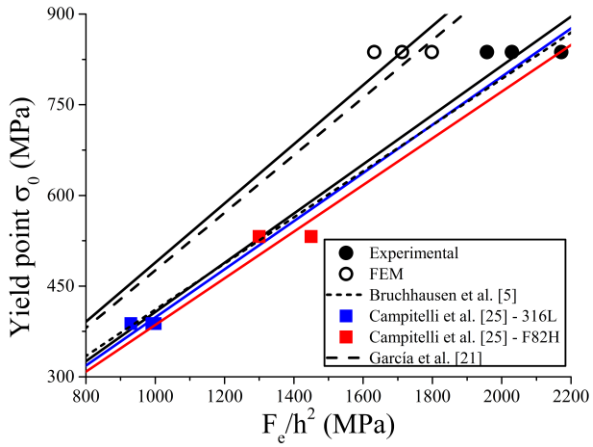

Fig. 12. Relations between F_e/h^2 and yield point σ_0 for experimental and numerical results in present study, compared with various literature data

The mean FEM-designated α value of 0.488 is closely related to the results reported by [30], where mean $\alpha = 0.475$ parameter was averaged for various alloys (including high strength, structural and stainless steels). It confirms that $\alpha = 0.475$ is indeed a good estimate for plenty of materials. As can be seen in Tab. 3, mean experimental $\alpha = 0.407$, although within the range of values contributed by other authors, shows noticeable disagreement with FEM. This scatter is a consequence of discrepancies between calculated and experimental $F(u)$ responses, particularly in the elastic region. As mentioned earlier, the elastic slope of FEM curve is generally much steeper, which affects greatly position of the intersection point of the two lines (Fig. 4) and, subsequently, the transition point F_e evaluation (error remains in the order of 15%). Hence, particular caution should be kept when assessing σ_0 from numerical curves.

The relationship between the maximum SPT load and tensile strength was studied as well. In line with Altstadt et al. [23], the scatter between the FEM and experimental estimates of σ_{UTS} is generally smaller than in case of σ_0. Experimental β_1 is in average 5% lower than FEM value and both match well with the literature data. FEM calculations prove that normalising neither the Eq. 3 with h^2 nor Eq. 4 with $u_m h$ does not fully eradicate its thickness dependence, as they show clear linear correlation with h (Fig. 13).

Additional simulations were run to check the applicability of Eqs. 3 and 4 at varying test conditions, i.e. different indenter diameter. Other authors have already pointed out that the relationship between the SPT maximum load and ultimate strength depends strongly on test rig configuration and conditions, as these factors affect the F_{max} value markedly [3,28].

On the other hand, the incorporation of $u_m h$ into the Eq. 4 takes into account reduction of thickness (necking) occurring during the test and appears to, at least partly, compensate different test conditions factors [30]. In Fig. 14, the FEM curve ($h = 0.25$ mm, $\mu = 0.1$) obtained for nominal Ø 1 mm ball diameter used in experiment is compared with those obtained for Ø 0.8 and Ø 1.2 mm diameters.

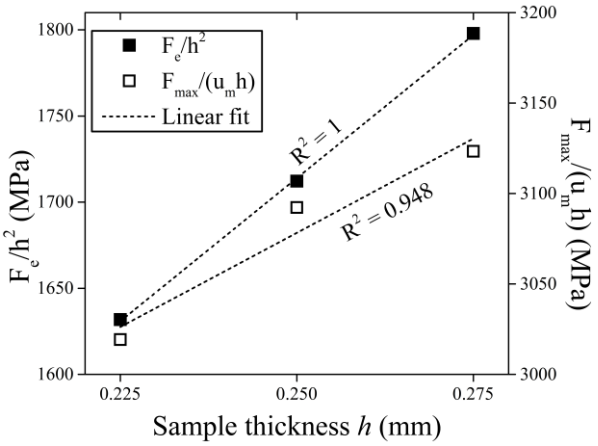

Fig. 13. Sample thickness dependence of F_e/h^2 and $F_{max}/(u_m h)$ expressions

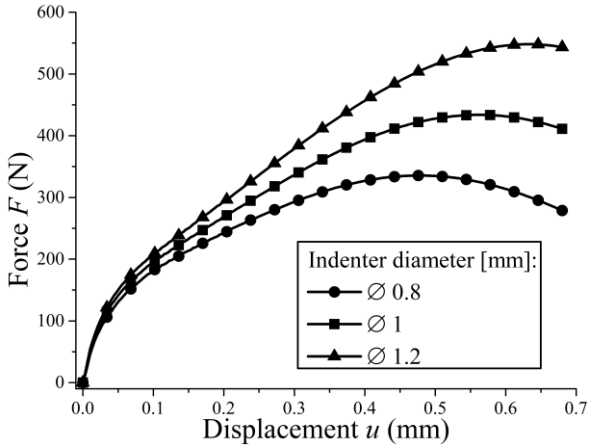

Fig. 14. Punch diameter influence on the shape of calculated load-displacement curves

As expected, the indenter diameter has remarkable influence on $F(u)$ response, particularly in the F_{max} region. The obtained data were processed analogously. As compared in Tab. 4, changing the ball diameter (in the $\pm$20 % range) has negligible influence on deriving yield properties. Hence, the presented method of assessing the yield point from SPT might be considered generalisable for the same material, even if the test conditions vary.

Tab. 4. Values of the factors used in Eqs. 3 and 4 obtained for various indenter diameter

Ball diameter [mm]	F_e/h^2 [MPa]	α	$F_{max}/(u_m h)$ [MPa]	β
Ø 0.8	1,688.9	0.496	2,819.5	0.337
Ø 1 (nominal)	1,712.2	0.489	3,092.3	0.307
Ø 1.2	1,708.4	0.490	3,466.8	0.274

Contrarily, it turned out that the relation between SPT maximum load and σ_{UTS} has to be viewed cautiously, as normalising it with $u_m h$ is insufficient to compensate differences in F_{max} caused by different punch diameters. Interestingly, the relationship between ball diameter and $F_{max}/(u_m h)$ expression presents linear correlation (Fig. 15).

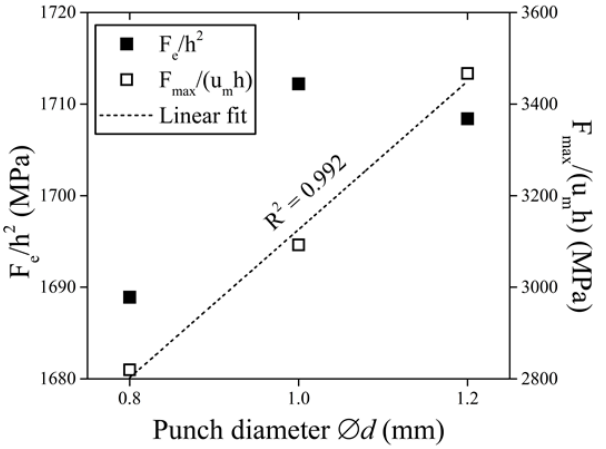

Fig. 15. Punch diameter dependence of $\mathrm{F_e/h^2}$ and $\mathrm{F_{max}/(u_m h)}$ expressions

Finally, a fractography study of tested specimens was done to determine failure micromechanisms. Fig. 16 represents the fracture surface of the broken 14Cr ODS steel after the SPT, observed in a scanning electron microscope (SEM). It may be assumed that the material exhibited mixed fracture mechanism, which is witnessed macroscopically by the coexistence of characteristic radial as well as circumferential (Fig. 16a) cracks on deformed surface. Presence of radial bursts indicates that cleavage is a predominant fracture mechanism, while ductile samples develop circumferential rupture along the sample-punch contact line [3,30]. Further evidence of hybrid fracture behaviour can be found at higher magnification observations, as dimples and cleavage planes occur simultaneously in the fracture zone (Fig. 16b).

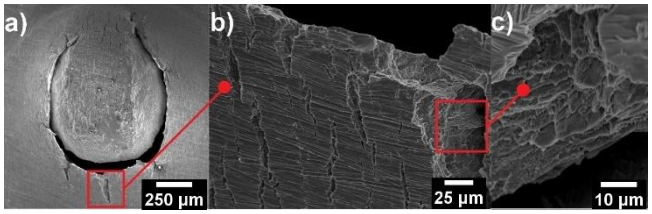

Fig. 16. SEM images of broken small punch 14Cr ODS steel specimen (details in text). SEM, scanning electron microscope; ODS, oxide-dispersion strengthened

4. CONCLUSION

Small punch and tensile tests have been performed at ambient temperature on a 14Cr ferritic ODS steel obtained via a PM route. The finite element model was developed and validated against TEM-sized (Ø 3 mm, $h = 0.25$ mm) ODS samples, which produced SPT responses comparable with experimental data. Strength parameters were extracted from the both FEM and experimental SPT results using the contemporary methodology and compared with the uniaxial tensile test results. The relations obtained for F_e/h^2 as well as for $F_{max}/(u_m h)$ are within the typical range of values found in the literature. It was proven that different ball diameter used in study has no remarkable influence on deriving yield properties, but produces large scatter in ultimate strength evaluation. Despite the fact that reliable assessment of mechanical properties from the SPT curve may be still regarded as challenging, mainly because of a complex stress state which develops in tested specimens, this study confirms that a great advancement has been made in this field recently.

On the basis of FEM simulations, it can be stated that friction belongs to the key factors affecting the results of the SPT, as it directly affects the shape of force-displacement curve and strain distribution across the sample. Necking of the specimen becomes pronounced at μ values exceeding 0.2. It was found that high friction not only increases the magnitude of peak strain but also moves its location away from the punch pole. This suggests that lubrication of the test parts may be desirable as it reduces the ultimate load and allows the strain to distribute more consistently.

REFERENCES

1. Corwin WR, Rosinski ST, van Walle E. Small Specimen Test Techniques. Philadelphia (PE): Society for Testing and Materials; 1998.
2. Chen H, Hyde TH. Use of multi-step loading small punch test to investigate the ductile-to-brittle transition behaviour of a thermally sprayed CoNiCrAlY coating. Mater Sci Eng A. 2017;680:203-209.
3. Contreras M, Rodríguez C, Belzunce FJ, Betegón C. Use of the small punch test to determine the ductile-to-brittle transition temperature of structural steels. Fatigue Fract Eng Mater Struct. 2008;31(9):727-737.
4. Jaya BN, Alam Z. Small-scale mechanical testing of materials. Curr Sci. 2013;105(8);1073-1099.
5. Bruchhausen M, Holmström S, Simonovski I, Austin T, Lapetite J-M, Ripplinger S, de Haan F. Recent developments in small punch testing: Tensile properties and DBTT. Theor Appl Fract Mech. 2016;86(A):2-10.
6. Oksiuta Z, Lewandowska M, Kurzydłowski KJ. Mechanical properties and thermal stability of nanostructured ODS RAF steels. Mech Mater. 2013;67:15-24.
7. Okuda N, Kasada R, Kimura A. Statistical evaluation of anisotropic fracture behavior of ODS ferritic steels by using small punch tests, J Nucl Mater. 2009;386-388:974-978.
8. Shimomura Y, Spears W. Review of the ITER Project, IEEE Trans Appl Supercond. 2004;14(2):1369-1735.
9. Motojima O. The ITER project construction status. Nucl Fusion. 2015;55(10):104023.
10. Zinkle SJ. Challenges in Developing Materials for Fusion Technology - Past, Present and Future. Fusion Sci Technol. 2017;64(2):65-75
11. Zhao Q, Ma Z, Yu L, Li H, Liu C, Li C, Liu Y. Tailoring the secondary phases and mechanical properties of ODS steel by heat treatment. J Mater Sci Technol. 2019;35(6):1064-1073.
12. Zhang L, Yu L, Liu Y, Liu C, Li H, Wu J. Influence of Zr addition on the microstructures and mechanical properties of 14Cr ODS steels. Mater Sci Eng A. 2017;695:66–73.
13. Li W, Hao T, Gao R, Wang X, Zhang T, Fang Q, Liu C. The effect of Zr, Ti addition on the particle size and microstructure evolution of yttria nanoparticle in ODS steel. Powder Technol. 2017;319:172–182.
14. Oksiuta Z, Mueller P, Spätig P, Baluc N. Effect of thermo-mechanical treatments on the microstructure and mechanical properties of an ODS ferritic steel. J Nucl Mater. 2011;412(2): 221-226.
15. Oksiuta Z, Ozieblo A, Perkowski K, Osuchowski M, Lewandowska M. Influence of HIP pressure on tensile properties of a 14Cr ODS ferritic steel. Fusion Eng Des. 2014;89(2):137-141.
16. Li Y, Shen J, Li F, Yang H, Kano S, Matsukawa Y, Muroga T. Effects of fabrication processing on the microstructure and mechanical prop-

DOI 10.2478/ama-2022-0027

erties of oxide dispersion strengthening steels. Mater Sci Eng A. 2016;654:203-212.
17. Zhao Q, Yu L, Liu Y, Huang Y, Ma Z, Li H, Wu J. Microstructure and tensile properties of a 14Cr ODS ferritic steel. Mater Sci Eng A. 2017;680:347-350.
18. De Sanctis M, Fava A, Lovicu G, Montanari R, Richetta M, Testani C, Varone A. Mechanical Characterization of a Nano-ODS Steel Prepared by Low-Energy Mechanical Alloying. Metals. 2017;7(8): 283.
19. Murty K, Charit I. An Introduction to Nuclear Materials: Fundamentals and Applications. Weinheim (DE): Wiley-VCH; 2013.
20. Karthik V, Kasiviswanathan KV, Raj B. Miniaturized Testing of Engineering Materials. Boca Raton (FL): CRC Press; 2017.
21. Simonovski I, Holmström S, Bruchhausen M. (2017), Small punch tensile testing of curved specimens. Int J Mech Sci. 2017;120: 204-213.
22. Manahan M, Argon A, Harling O. The development of a miniaturised disk bend test for the determination of postirradiation mechanical properties. J Nucl Mater. 1981;104:1545-1550.
23. Altstadt E, Ge HE, Kuksenko V, Serrano M, Houska M, Lasan M, Bruchhausen M, Lapetite J-M, Dai Y. Critical evaluation of the small punch test as a screening procedure for mechanical properties. J Nucl Mater. 2016;472:186-195.
24. Lucon E, Benzing J, Hrabe N. Development and Validation of Small Punch Testing at NIST. Gaithersburg (MD): National Institute of Standards and Technology; 2020. doi: 10.6028/NIST.IR.8303
25. Yang SS, Ling X, Qian Y, Ma RB. Yield Strength Analysis by Small Punch Test Using Inverse Finite Element Method. Procedia Eng. 2015;130:1039-1045.
26. Moreno MF, Bertolino G, Yawny A. The significance of specimen displacement definition on the mechanical properties derived from Small Punch Test. Mater Des. 2016;95, 623–631.
27. Sánchez-Ávila D, Orozco-Caballero A, Martínez E, Portolés L, Barea R, Carreño F. High-accuracy compliance correction for nonlinear mechanical testing: Improving Small Punch Test characterization. Nucl Mater Energy. 2021;26:100914.
28. Campitelli EN, Spätig P, Bonadé R, Hoffelner W, Victoria M. Assessment of the constitutive properties from small ball punch test: experiment and modelling. J Nucl Mater. 2004;335(3):366–378.
29. Kalidindi SR, Abusafieh A, El-Danaf E. Accurate characterization of machine compliance for simple compression testing. Exp Mech. 1997;37(2);210–215.
30. García TE, Rodríguez C, Belzunce FJ, Suárez C. Estimation of the mechanical properties of metallic materials by means of the small punch test. J Alloys Compd. 2014;582:708–717.
31. Mao X, Takahashi H. Development of a further-miniaturized specimen of 3 mm diameter for tem disk (ø 3 mm) small punch tests. J Nucl Mater. 1987;150(1):42–52.
32. Prakash RV, Arunkumar S. Influence of Friction on the Response of Small Punch Test. Trans Indian Inst Met. 2016;69(2):617-622.
33. Haroush S, Priel E, Moreno D, Busiba A, Silverman I, Turgeman A, Gelbstein Y. Evaluation of the mechanical properties of SS-316L thin foils by small punch testing and finite element analysis. Mater Des. 2015;83:75-84.

Acknowledgements: This work is supported by the Ministry of Science and Higher Education of Poland under research project No. WI/WM-IIM/3/2022.

Krzysztof Nowik: https://orcid.org/0000-0003-3523-9786

Zbigniew Oksiuta: https://orcid.org/0000-0002-8719-157X